# Experimental and modelling results of the QUENCH-20 experiment with BWR test bundle

Juri Stuckert [a,*], Sevostian Bechta [b], Thorsten Hollands [c], Patrick Isaksson [d], Martin Steinbrueck [a]

[a] Karlsruhe Institute of Technology (KIT), Germany
[b] Kungliga Tekniska högskolan (KTH), Sweden
[c] Gesellschaft für Anlagen- und Reaktorsicherheit (GRS), Germany
[d] Strålsäkerhetsmyndigheten (SSM), Sweden

*Keywords:*
Severe accident
Neutron absorber
Eutectic formation
Reflood
Melt relocation and oxidation
Hydrogen release

A B S T R A C T

The experiment QUENCH-20 with BWR simulation bundle was conducted at KIT on 9th October 2019. This test was performed in the framework of EU SAFEST project and its international access to European SA research infrastructure of the users from Swedish Radiation Safety Authority (SSM) in collaboration with Westinghouse Sweden, GRS and KTH. The test objective was the investigation of the BWR fuel assembly degradation including a control blade with $B_4C$ neutron absorbers. The test bundle represented one quarter of a BWR fuel assembly. 24 electrically heated fuel rod simulators were filled with krypton (pressure of about 0.6 MPa), whereas the holes of absorber pins were filled with helium (overpressure 0.02 MPa). According to the pre-test calculations performed with ATHLET-CD, the bundle was heated to a temperature of 1230 K at the cladding of the central rod at the hottest elevation of 950 mm. This pre-oxidation phase in steam lasted 4 h. During the following transient stage, the bundle was heated to a maximal temperature of 2000 K. The cladding failures were observed at temperatures about 1700 K and lasted about 200 s. Massive absorber melt relocation was observed 50 s before the end of the transient stage. The test was terminated by the injection of quench water with a flow rate of 50 g/s into the bundle bottom. Fast temperature escalation from 2000 to 2300 K during 20 s was observed. The mass spectrometer measured release of $CO_x$ and little $CH_4$ during the reflood as products of absorber oxidation; corresponding mass of reacted $B_4C$ was 4.3% of the total mass of $B_4C$ pins. Hydrogen production during the reflood amounted to 32 g (57.4 g during the whole test) including 10 g from $B_4C$ oxidation. The results of the post-test simulations with the AC$^2$/ATHLET-CD code show a good agreement with the experimental observations concerning the thermal behavior. However, melting and relocation of BWR components was not calculated and the $B_4C$ oxidation was underestimated.

## 1. Introduction

The main goal of the QUENCH program at KIT is to investigate the core thermal response, the oxidation of cladding tubes and absorber materials with accompanying hydrogen release as well as the cooling efficiency of water injection under design basis (DBA) and beyond design basis (BDBA) accident conditions. The program was initiated in 1996 and is still on-going (Hering and Homann, 2007; Steinbrück et al., 2010; Stuckert et al., 2013). Experiment QUENCH-20 on high temperature behavior of BWR materials was performed on 9th October 2019 (Stuckert et al., 2022) in the framework of EU SAFEST project (Miassoedov et al., 2017) and its international access to European SA research infrastructure of the users from Swedish Radiation Safety Authority (SSM) in cooperation with Westinghouse Sweden, GRS and KTH. QUENCH-20 was the worldwide first bundle experiment with ¼ SVEA-96 OPTIMA2 assembly simulator including control elements consisting of two stainless steel blades with inserted $B_4C$ pins.

Two of the early QUENCH bundle experiments on severe accident were performed with *PWR* geometry containing a central $B_4C$ neutron absorber rod: QUENCH-07 (Steinbrück et al., 2004) and QUENCH-09 (Steinbrück et al., 2004; Homann et al., 2006). Similar to previous CORA tests (Schanz et al., 1992; Hagen et al., 1996.; Ott and Hagen, 1997; Haste et al., 2015) with BWR bundles, these experiments showed degradation of absorber materials due to eutectic interactions $B_4C$-

* Corresponding author at: Hermann-von-Helmholtz-Platz 1, 76344 Eggenstein-Leopoldshafen, Germany.
*E-mail address:* juri.stuckert@kit.edu (J. Stuckert).

stainless steel-zirconium already before reflood. The total oxidation of $B_4C$ during QUENCH-07 was ≈20% and occurred mostly during reflood; the hydrogen resulting from the $B_4C$ oxidation was analyzed to be ≈4.3 g, or 2.4% of the total $H_2$ produced (186 g). The evaluation of the QUENCH-09 tests conducted partially under steam starvation conditions showed that no significant amount of reaction products of the $B_4C$ oxidation was generated before cooling initiation and the total amount of CO and $CO_2$ was almost completely produced during the reflood phase. Based on the total amounts of CO and $CO_2$ (33 and 22 g, respectively) the contribution of $B_4C$ oxidation to hydrogen formation was evaluated as 2.2% of integral mass of 460 g during QUENCH-09 test. The fraction of the $B_4C$ mass that was oxidized during the QUENCH-09 test was evaluated to be ≈50%. The results obtained in the bundle tests correspond well with the results obtained in separate-effects tests on boron carbide oxidation and gas production (Steinbrück, 2010). The main reaction products of the $B_4C$ oxidation are $H_2$, CO, $CO_2$, and boric acids $HBO_2$ and $H_3BO_3$. Only very limited amounts of methane $CH_4$ were produced at the high temperatures in the bundle. This is in agreement with thermo-chemical equilibrium calculations, which predict significant methane production only below 600–700 °C.

While the processes of degradation of neutron absorber materials in PWRs have been studied in sufficient details (Steinbrück, 2014), the amount of research on this problem for BWRs has remained relatively small until recently. Of the nineteen CORA experiments, only six were performed with BWR control rods (Schanz et al., 1992). Fukushima-Daiichi accident stimulated new studies in this area. In Japan, a number of relevant experiments were carried out, but the absorber material was placed in vertical stainless-steel claddings (Pshenichnikov et al., 2021). There is another type of absorber design of the SVEA-96 OPTIMA2 assemblies having $B_4C$ pins in horizontal holes of stainless steel blades. It was decided to carry out the QUENCH-20 experiment representing the SVEA control rod design.

## 2. Test facility and instrumentation

The general scheme of the QUENCH test section is given in Fig. 1. QUENCH-20 was conducted in forced-convection mode, in which superheated steam from the steam generator and superheater together with argon as a carrier and reference gas for off-gas measurements enter the test bundle at the bottom.

The gases injected or produced during the test flow from the bundle outlet at the top through a water-cooled off-gas pipe to the condenser where the steam is separated from the non-condensable gases. The water cooling circuits for bundle head and off-gas pipe are temperature-controlled to guarantee that the steam temperatures are high enough to avoid condensation at the test section outlet and inside the off-gas pipe and to allow quantitative measurements of steam concentration by mass spectrometer.

The test rods were arranged within the QUENCH-20 bundle as shown in the schematic cross section of Fig. 2. The test bundle represented one quarter of a BWR fuel assembly. The rod cladding of the fuel rod has 9.84 mm outside diameter and 8.63 mm inner diameter. The cladding tubes used in this test consisted of Zircaloy-2 with inner liner (LK3/L). The test bundle is approximately 2.5 m long and is made up of 24 heated fuel rod simulators. Heating is electric by 5.25 mm diameter tungsten heaters installed in the rod centers. The bundle section is heated by the tungsten heaters between bundle elevations 0 and 1024 mm. Molybdenum heaters and copper electrodes are connected to the tungsten heaters at one end and to the cable leading to the DC electrical power supply at the other end. Two DC generators were applied; the corresponding bundle partitioning (12 + 12 rods) between two generators is marked in Fig. 2 with two transparent colors. The tungsten heaters are surrounded by annular $ZrO_2$ pellets simulating $UO_2$ fuel. The Mo heaters and Cu electrodes are coated with a $ZrO_2$ layer (about 200 μm thick) to avoid electrical contact to the cladding inner surface. All the test rods were filled with Kr at a pressure of approximately 0.6 MPa after bundle

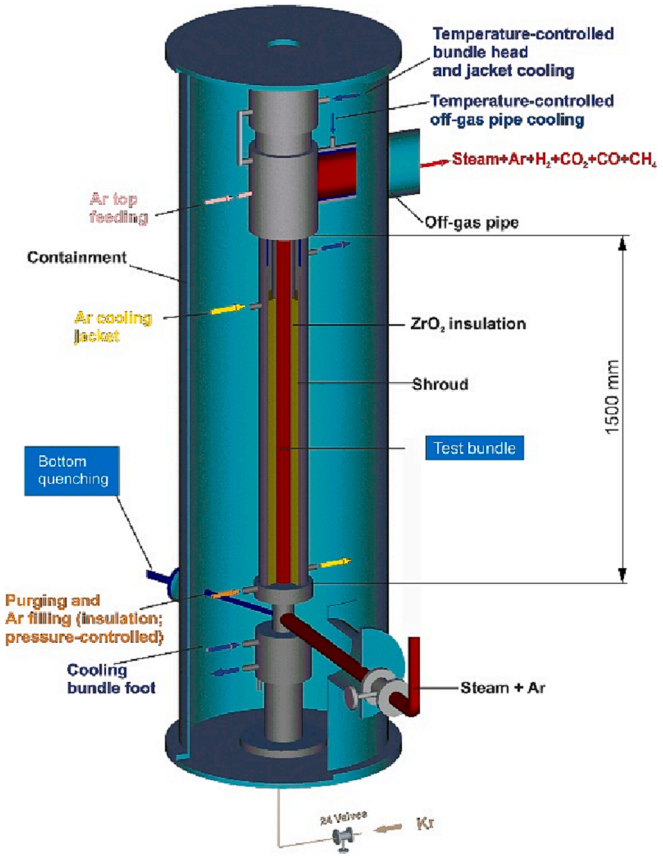


**Fig. 1.** QUENCH facility (Stuckert et al., 2022).

heating to cladding peak temperature of 900 K. The system pressure maintained at about 0.2 MPa.

The fuel rod simulators are held in position by five grid spacers at bundle elevations 200, 50, 550, 1050 and 1410 mm. All five grid spacers were the standard Westinghouse Inconel X750 spacers.

Two steel blades (total mass 7.4 kg, length of each 1.56 m) with horizontal *$B_4C$ absorber pins* (total mass 0.875 kg, or 10.6% by weight or 23% by volume filling ratio of $B_4C$ in the control rod) were filled with helium (0.12 MPa) and inserted between channel box, made of low tin ZIRLO alloy with about 0.66% Sn, and shroud. The composition of the steel blade is the following (low carbon alloy AISI 316L SS): Fe, Cr (17%), Ni (11%), Mo (2.5%), [Si, P, S (<1%)], C (0.03%).

One Zircaloy-4 corner rod was installed in the water channel and was designed to be withdrawn from the bundle to check the amount of oxidation and hydrogen absorption at a specific time. This corner rod was withdrawn at the end of the pre-oxidation stage.

The test bundle is surrounded by an octagonal shroud made of Zr 702 ((Zr + Hf) 99.2%, Hf 4.5%, (Fe + Cr) 0.2%, H 0.005%, N 0.025%, C 0.05%, O 0.16%), then by $ZrO_2$ fiber insulation extending from the bottom (-300 mm) to the upper end of the heated zone (+1024 mm) and a double-walled cooling jacket made of Inconel 600 (inner)/stainless steel (outer) over the entire length.

The annulus between shroud and cooling jacket with the fiber insulation is purged (after several cycles of evacuation) and then filled with stagnant argon. The annulus is connected to a flow- and pressure-controlled argon feeding system in order to keep the pressure constant at the target of 0.3 MPa (beyond this pressure gas is released by the feeding system). This should prevent an access of steam from the test bundle (with a system pressure of 0.2 MPa) to the annulus after a possible shroud failure, after which argon is supplied continuously into the annulus.

The 6.7 mm annulus of the cooling jacket is cooled by argon flowing

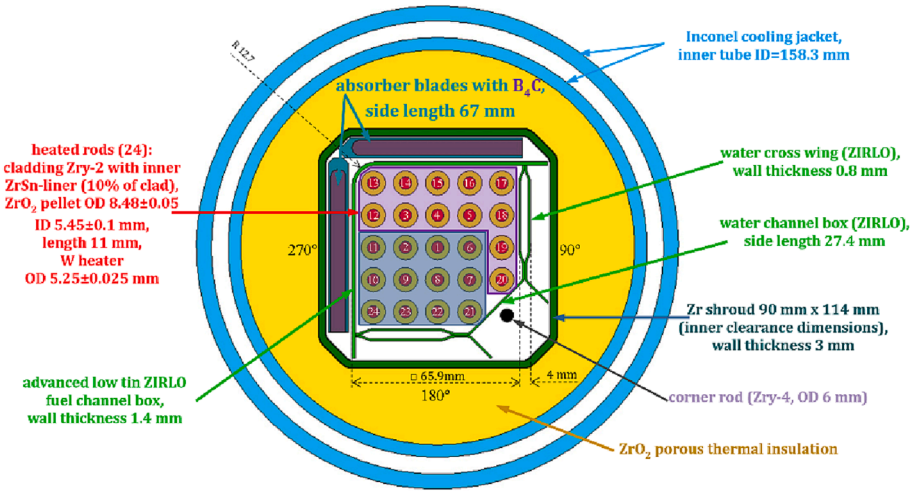


**Fig. 2.** Bundle cross section.

from the upper end of the heated zone to the bottom of the bundle and by water in the upper electrode zone. Both the absence of $ZrO_2$ insulation above the heated region and the water cooling are to avoid too high temperatures of the bundle in that region.

All measurement devices used in QUENCH-20 were connected to the MERSY/Siemens measurement system. The readings of pressure transducers connected to each rod were recorded separately by the DELPHIN measurement system. For temperature measurements, the test bundle, shroud, and cooling jackets are equipped with thermocouples. The thermocouples attached to the outer surface of the rod cladding at elevations between –250 and + 1350 mm are designated "TFS" for all heated rods. The shroud thermocouples (designation "TSH") are mounted at the outer surface between –250 and + 1250 mm. The thermocouples installed at the blade side at the bundle elevations 250, 350 and 450 mm are designated as TBL. The thermocouples mounted at the channel box at elevations 350 and 450 mm are designated as TCH.

The thermocouples in the lower bundle region, i.e. up to 550 mm elevation, were NiCr/Ni thermocouples with stainless steel sheath/MgO insulation and an outside diameter of 1.0 mm, used for measurements of the rod cladding and shroud temperatures. The thermocouples in the hot zone and above were high-temperature thermocouples with W5Re/W26Re wires, $HfO_2$ insulation, and two sheaths of tantalum (inner sheath) and zirconium (outer sheath). The high temperature thermocouples have an outer diameter of about 2.3 mm and were welded to the outer surface of claddings and shroud with Zr clamps.

The gas release is analyzed by a quadrupole mass spectrometer Balzers "GAM300" with the sampling position at the off-gas pipe of the test facility. Ion currents were measured at selected masses of all relevant gases and converted into concentrations using calibration factors determined before the experiment. From these data, the mass production rate of hydrogen as well as of the other gases is calculated with the ratio of the concentrations of the particular gas and that one of argon (carrier gas) and multiplied by the argon flow rate through the test bundle. The uncertainty for the gas release rate is about 0.004 mol/$m^2$/s. The delay time for the gas transfer from the hottest bundle elevation to the mass spectrometer is about 5 s.

## 3. Test performance and results of online measurements

In the QUENCH-20 experiment, the test sequence can be distinguished in the following stages:

*1) Pre-oxidation* 0 – 14416 s, 2) *Transient* 14,416 – 15882 s, 3) *Reflood* 15,882 – 16375 s.

The scheme of test performance is depicted in Fig. 3. The *pre-oxidation stage* in a flowing gas mixture of steam and argon lasted 4 h at the peak cladding temperature of approximately 1250 K, i.e. below the

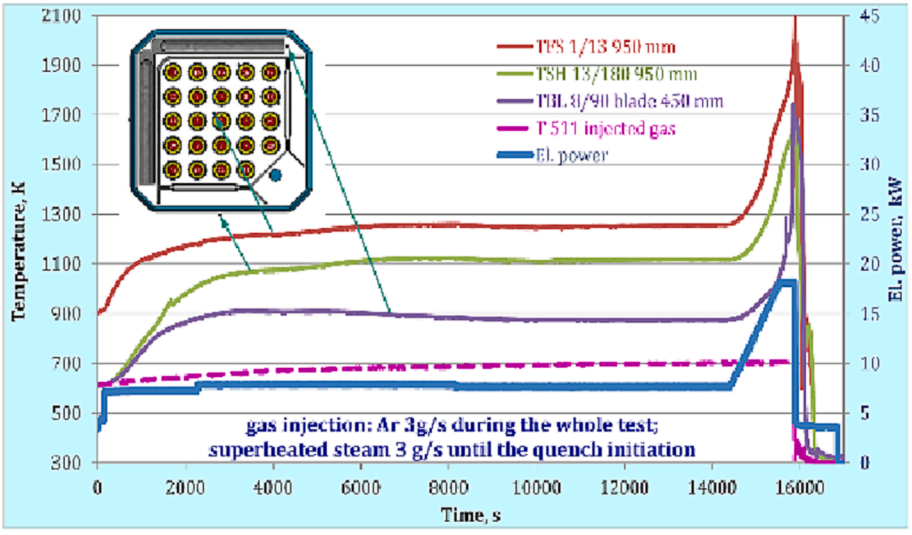


**Fig. 3.** Heating power and temperature evolution.

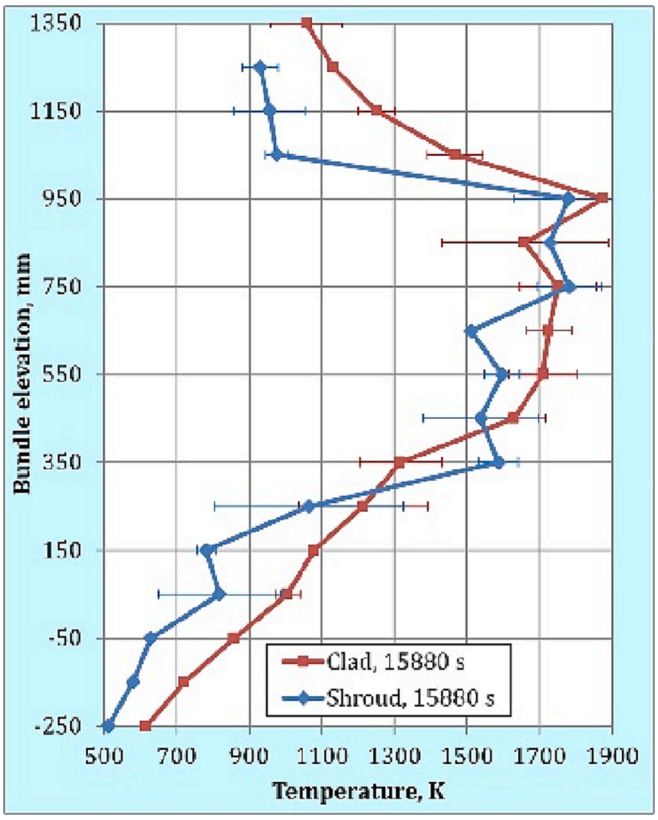


**Fig. 4.** Axial temperature profiles of outer cladding surfaces at the end of temperature escalation.

$B_4C$-SS eutectic temperature. The corner rod, withdrawn at the end of this stage, showed the maximal oxidation up to 60 μm $ZrO_2$ between elevations 930 and 1020 mm and only 10 μm at 750 mm. This corresponds to the typical values of the maximum and average oxidation of the claddings observed in BWR at high burnups (Fig. 3.7a in (IAEA-TECDOC-684, 1993).

During the *transient stage*, the bundle was heated to a maximum cladding temperature of 2000 K, i.e. slightly below the melting point of the beta phase of Zircaloy (about 2030 K). Simultaneous registration of the drop in internal rod pressure and the release of krypton made it possible to conclude about the conditions of the cladding failures. It was determined that the cladding ruptures occurred firstly during the transient for approximately 200 s as the cladding temperature reached approximately 1700 K at the hottest elevation of 950 mm.

To determine the axial temperature profile at a certain time, the average values of all thermocouple readings of certain bundle elevation were derived separately for claddings and shroud. Fig. 4 presents these axial temperature distributions at the end of the transient stage. The hottest elevation of QUENCH-20 was the level 950 mm similar to most former QUENCH bundle tests. However, this maximum is not very pronounced and there is a certain flat range of temperatures between the bundle elevations of 450 and 850 mm. Elevated temperatures in this extended segment of the bundle can be associated with the relocation of the eutectic melt of absorber materials formed at higher elevations at $T > 1500$ K. This can be confirmed by sharp temperature jumps near the absorber materials at the lower bundle elevations. Fig. 5 demonstrates this fact by presenting the readings of the respective thermocouples set between 250 and 450 mm: the melt relocated from above leads to an abrupt temperature increase at 15680…15720 s. At the same time, small release of $CH_4$ (as $B_4C$ oxidation product) was recorded (Fig. 7).

The *reflood stage* was started with quench water injection with the flow rate of 50 g/s at 15891 s after fast filling of the bundle foot with 4 L water at 15882 s and simultaneous reduction of electric power from 18.2 kW to simulated decay power of 4 kW. Within 20 s after the initiation of the reflood, an intense escalation of temperatures was observed at elevations of 750…950 mm. In this case, the maximum temperature measured on the surface of the claddings was 2098 K at the elevation of 950 mm (thermocouple TFS 1/13 located at the cladding outer surface of the rod #1). The maximum cladding temperatures at the elevations of 750 and 850 mm could not be measured, since a number of corresponding thermocouples failed after the reflood. The thermocouples located on the outer surface of the shroud remained intact, showing the highest temperatures up to *2500 K* on the outer surface of the shroud at the elevation of 750 mm (Fig. 6).

In addition to the exothermic oxidation of the surface of the cladding tubes (which by this time were already quite strongly oxidized), two other reasons for such a strong increase in temperatures can be 1) exothermic oxidation of the above-mentioned eutectic melt of the absorber materials, 2) direct oxidation of $B_4C$ pins, also accompanied with intense exothermic reactions. Indeed, during the quench stage, the

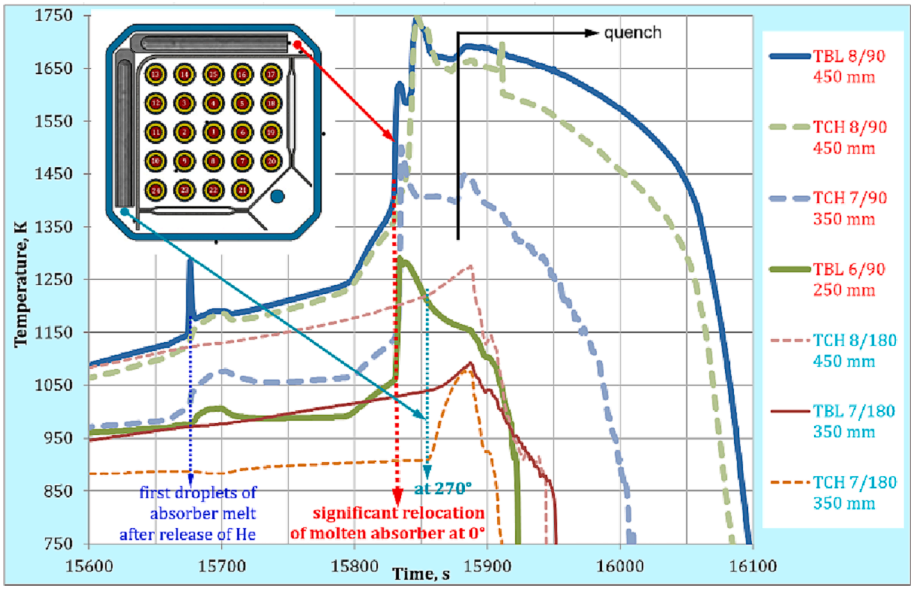


**Fig. 5.** Abrupt temperature increases at the lower bundle elevations between 250 and 450 mm due to the eutectic absorber melt relocated from higher elevations.

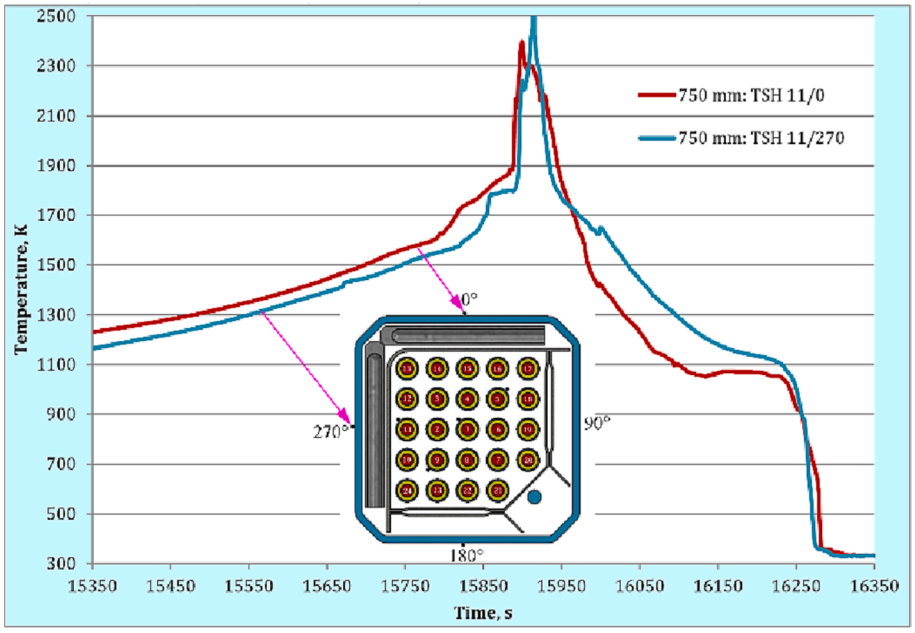


**Fig. 6.** Temperature escalation at 750 mm after reflood initiation at 15981 s.

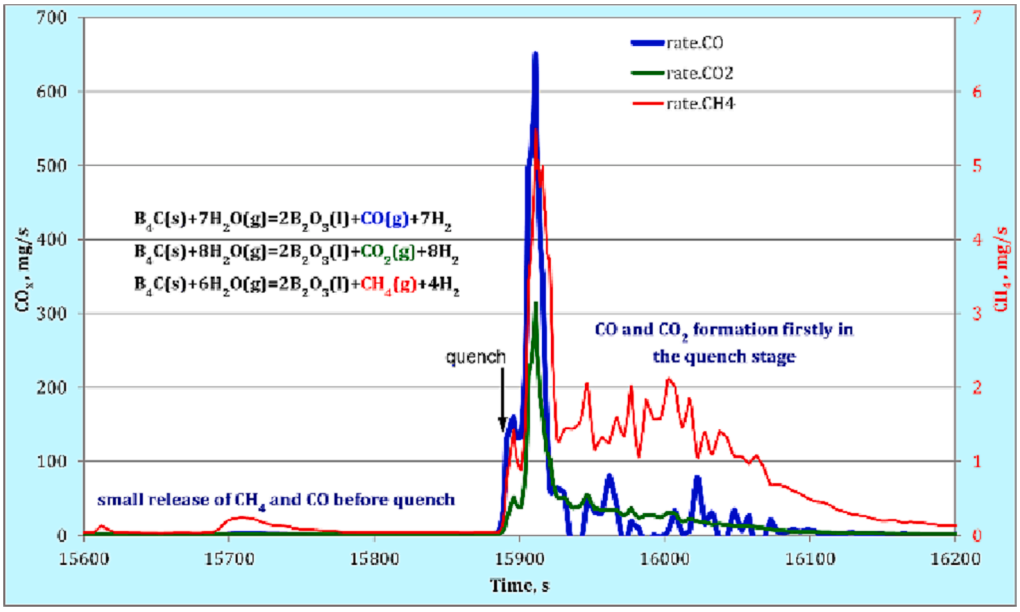


**Fig. 7.** Generation rates of carbon gases due to $B_4C$ oxidation by steam.

mass spectrometer registered release of the following products of $B_4C$ oxidation by steam: significant amounts of CO (12.6 g), and $CO_2$ (9.7 g) as well as a relatively small mass of $CH_4$ (0.4 g), see Fig. 7 and Fig. 8. This corresponds to the following chemical reactions (heat of reaction according to (Barin, 1995):

$$B_4C + 7H_2O = 2B_2O_3 + CO + 7H_2 + [732\ kJ/mol\ @\ 1600\ K] \quad (1)$$

$$B_4C + 8H_2O = 2B_2O_3 + CO_2 + 8H_2 + [761\ kJ/mol @ 1600\ K] \quad (2)$$

$$B_4C + 6H_2O = 2B_2O_3 + CH_4 + 4H_2 + [959\ kJ/mol\ @ 1600\ K] \quad (3)$$

Steam reacts with liquid boron oxide to form volatile boric acids:

$$B_2O_3 + H_2O = 2HBO_2 \quad [329\ kJ/mol @ 1600\ K] \quad (4)$$

$$B_2O_3 + 3H_2O = 2H_3BO_3 + [42\ kJ/mol @ 1600\ K] \quad (5)$$

Boron oxide itself directly evaporates at temperatures above 1500 °C. Theoretically, two additional reactions are possible:

$$CO + H_2O \rightleftharpoons CO_2 + H_2 + [29\ kJ/mol\ @\ 1600\ K] \quad (6)$$

$$CH_4 + H_2O \rightleftharpoons CO + 3H_2 \quad [217\ kJ/mol\ @\ 1600\ K] \quad (7)$$

The reaction (6) is the so called a water–gas shift reaction (WGSR), which is moderately exothermic and shifts towards reactants with growing temperatures. I.e. at high temperatures (QUENCH-conditions), the production of a noticeable amount of hydrogen thermodynamically is less favorable. The reaction (7) is a strongly endothermic reaction, which is possible above 700 °C only in the presence of nickel as catalyst. The probability of production of additional hydrogen due to this

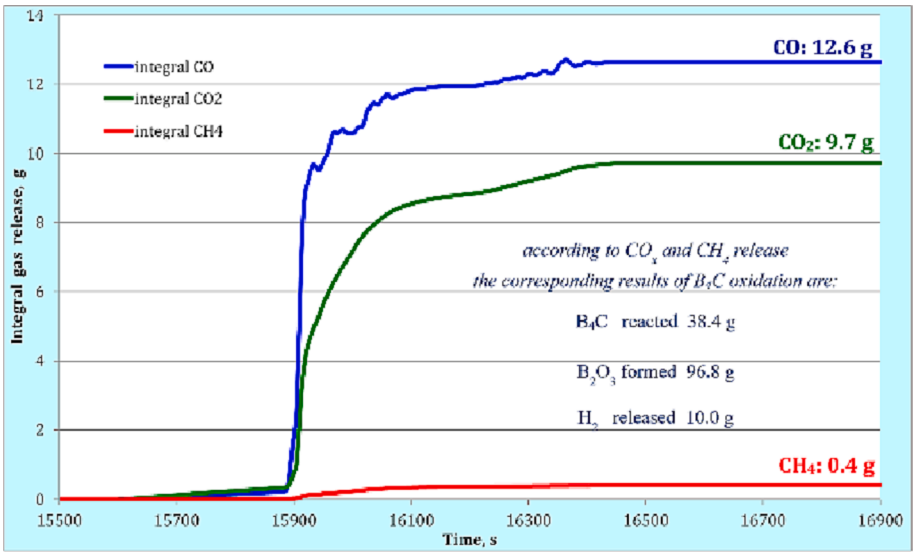


**Fig. 8.** Integral gas release due to oxidation of $B_4C$.

reaction is also low for the QUENCH conditions (only the Inconel spacers have a noticeable content of Ni).

The calculations, based on the equations (1)…(3) and measured data, show that the corresponding mass of reacted $B_4C$ was 38.4 g (4.3% of the total mass of $B_4C$ pins). In addition to the released gases CO (12.6 g), $CO_2$ (9.7 g) and $CH_4$ (0.4 g), 96.8 g $B_2O_3$ were formed and 10 g hydrogen were released. The total energy release due to boron carbide oxidation is about 500 kJ. The amount of carbon-containing gases that have arisen due to the oxidation of carbon in the steel of the blades can be neglected, since the amount of carbon in the steel is only about 1% of the carbon in the $B_4C$ pins.

The integral hydrogen release recorded by the mass spectrometer during the whole test was 57.40 ± 0.17 g, of which 32 g during the quench stage (Fig. 9). Thus, 22 g of hydrogen was released during the reflood stage due to the interaction of steam with zirconium alloys and partially melted steel blades of the absorber. Assuming that all this hydrogen was associated only with the oxidation of zirconium, and taking into account that in this process 298.5 kJ heat per mole of hydrogen were released, this would correspond to a heat output of about 3300 kJ.

In sum, the estimated value of the chemical energy released due to the oxidation of the materials of the bundle and the absorber during a short period of escalation at the beginning of the reflood (about 20 s) is about 3800 kJ. A similar amount of energy was released during the last 200 s of electrical heating before the reflood. The result was the melting of the metal part of the claddings in the upper parts of the bundle, which was confirmed by metallographic investigations.

After the cessation of the temperature escalation, a period of gradual cooling of the bundle by rising water began. The initial oscillation readings of differential pressure transducer used for measurement of collapsed water level (Fig. 10) indicate intensive evaporation of quench water already during the first 150 s after reflood initiation. This was also registered by mass spectrometer, which showed an average steam release of about 30 g/s during this time. Due to very high temperatures, boiling occurred in the entire volume of the supplied water, turning it into a two-phase fluid. As a result, at the elevation of 650 mm, this fluid briefly wet the thermocouples. After the gradual cooling of the system, a waterfront was formed at levels of 550–600 mm. With the rise of this front, the final wetting of the thermocouples attached to the claddings began to occur. The sequence of final thermocouple wettings by a rising water front shows, that the bundle was cooled during about 450 s.

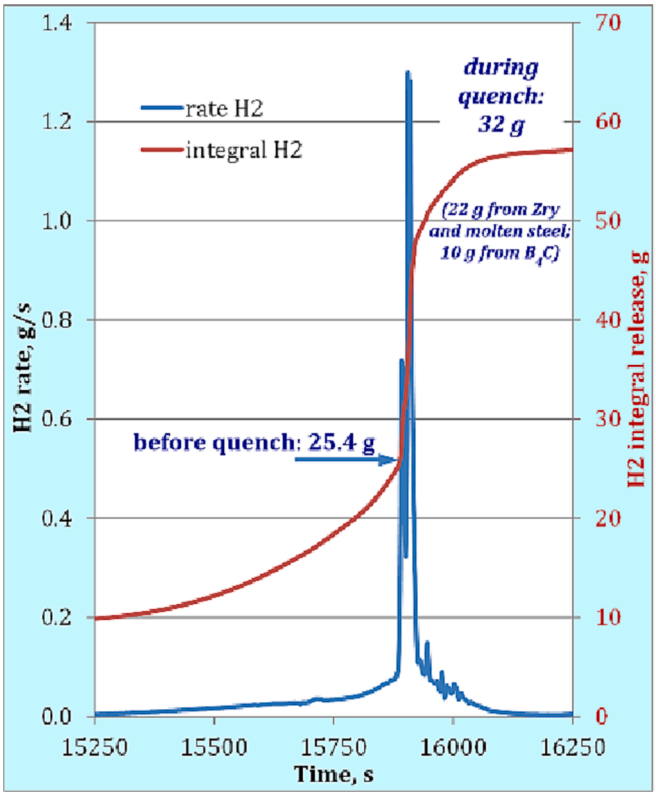


**Fig. 9.** Release rates and cumulative release of hydrogen during QUENCH-20.

## 4. Posttest investigations

Visual inspection of the bundle after being freed from the $ZrO_2$ thermal insulation showed severe damage of the shroud and the channel box between elevations 600 and 950 mm at the angle positions of the absorber blades (Fig. 11). At these bundle elevations, eutectic interaction between the $B_4C$ pins and the surrounding stainless steel blades took place leading to partial dissolution of boron and carbon in metallic melt. The formed melt has attacked the channel box and partially relocated to lower elevations inside the gaps between the rods and the channel box as well as between the channel box and the shroud.

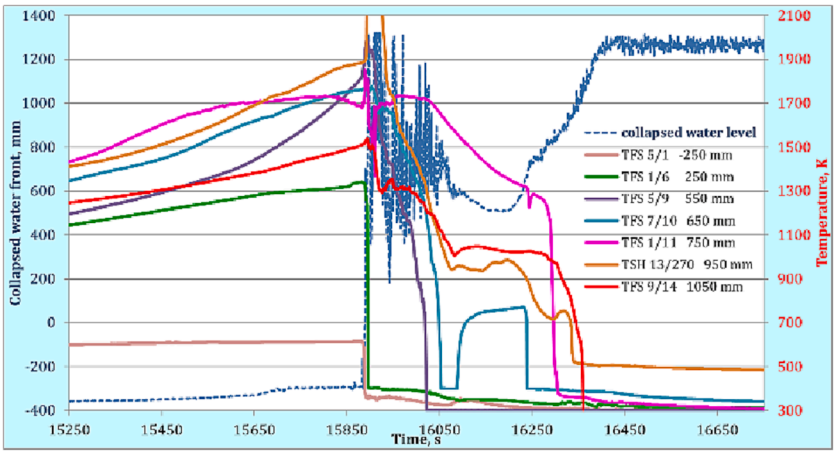


**Fig. 10.** Quench water level and wetting of thermocouple hot junctions.

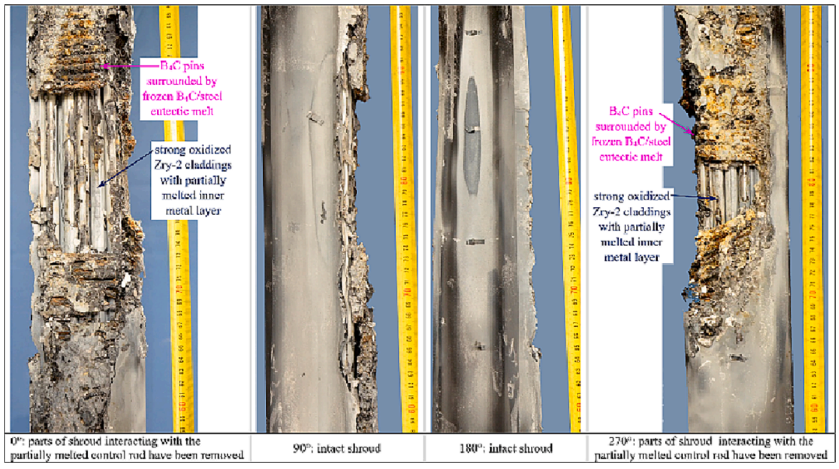


**Fig. 11.** Posttest view of bundle between 680 and 960 mm.

The test bundle was encapsulated in epoxy resin. After epoxy hardening during about three weeks, the bundle was cut into slices. Fig. 12 shows top views of ground and polished cross sections between elevations 250 and 1050 mm. The Zr elasticity decreases significantly at temperatures above 700 °C, consequently the shroud was ductile deformed during the pre-oxidation stage due to overpressure in the annulus outside the shroud (absolute pressure 0.3 MPa) in comparison to the bundle pressure of 0.2 MPa. This caused the bundle and two grid spacers (at 550 and 1050 mm) to be crushed in the 0° and 270° directions and led to the narrowing of the cooling channels between the rods. This, in turn, led to worse heat removal from the surface of the cladding tubes and contributed to the acceleration of the melting of the residual metal layers of the claddings. The cladding melt was partially released through the locally failed outer surface oxide into the space between rods at the bundle elevations 555…950 mm. The eutectic absorber melt is seen at elevations 450…950 mm. In the next sections, the features of the microstructure observed at individual elevations are described.

### 4.1. *Elevation 1050 mm*

A peak cladding temperature of about 1530 K was measured at the claddings of intermediate rods at the beginning of the quench stage. The absorber blades were partially melted due to eutectic interaction with the $B_4C$ pins. Due to the deformation of the bundle, the gap between the central rod and some rods surrounding it turned out to be minimal, which led to steam starvation in these places and the formation of only relatively thin oxide layers on the outer surface of the cladding (Fig. 13). The inner part of the β-Zr layer of the cladding is partially melted here due to the low heat removal. However, melting of the inner part of the cladding also occurred in some peripheral rods at locations that were in contact with adjacent rods (and, accordingly had poor heat removal at these locations). On the other hand, the relatively well cooled part of such cladding did not melt.

### 4.2. *Elevation 950 mm*

The peak cladding temperature about 2100 K was measured at the central rod during the quench stage. The absorber blade at the angle position 0° is heavily damaged due to eutectic interactions. The $B_4C$ pin


**Fig. 12.** Bundle cross sections at different elevations (arrows show regions with eutectic absorber melt).

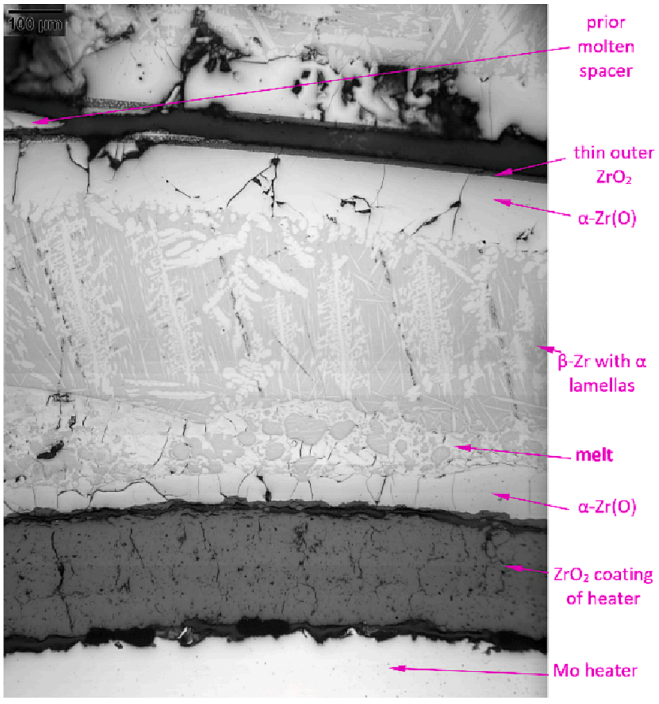


**Fig. 13.** Cladding microstructure of rod #1 (central rod) at 1050 mm.

is practically absent at this position, whereas the $B_4C$ pin at the angle position 270° was slightly attacked by the melt formed due to interaction of the stainless steel blade with the Zr-based channel box and the shroud.

Measurements of the thicknesses of the cladding layers, including outer and inner oxide and α-Zr(O) layers as well as primary β-Zr layers, showed that the thicknesses of the outer oxides correlate well with the overall oxidation of each rod. The averaged equivalent cladding reacted parameter determined using these measurements is ECR = 31%±8%. The degree of oxidation of the claddings is very inhomogeneous across the bundle (see Fig. 14 showing the averaged values of oxide thicknesses for each rod measured with a circumferential step of 45°). The

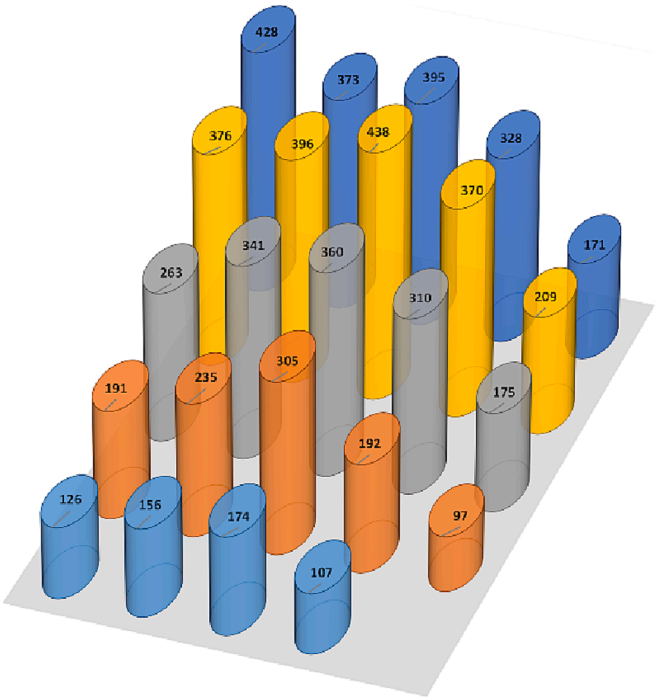


**Fig. 14.** Average thicknesses of outer $ZrO_2$ (in μm) for claddings at bundle elevation of 950 mm (top view).

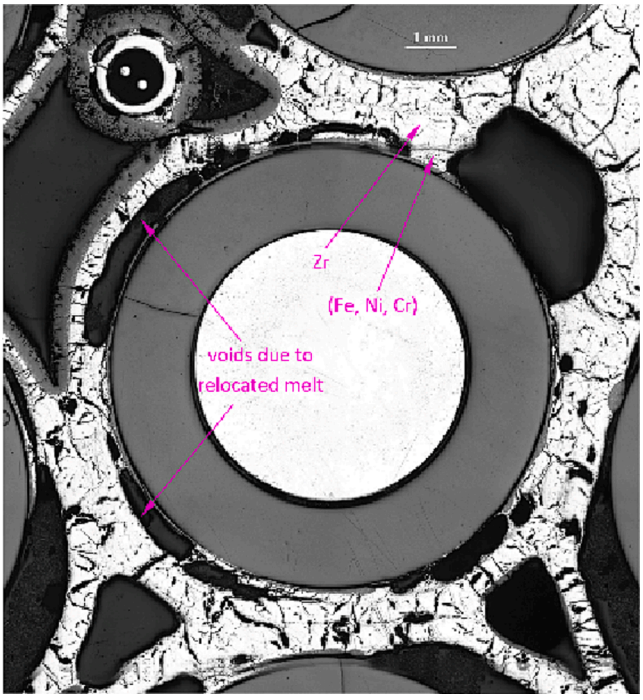


**Fig. 15.** Surrounding of rod #1 at 950 mm (top view).

distribution of oxide layers shows that the lowest temperatures were on those peripheral sides of the assembly where there were no absorber blades (bundle sides 90° and 180°). The highest cladding temperatures were reached in the corner region between the two absorber blades.

The gap between the pellets and the cladding was increased during the pre-oxidation stage due to the overpressure by the Kr filling gas (lift-off). The cladding melt was partially released outside the claddings of the inner rods 1…9 and mixed with the spacer melt and the absorber steel melt (Fig. 15). The inner cladding surface of several rods was also partially oxidized due to steam penetration in the gap or due to interaction with the $ZrO_2$ pellets. The claddings of peripheral hot rods along the absorber blades were strongly oxidized and partially melted. The

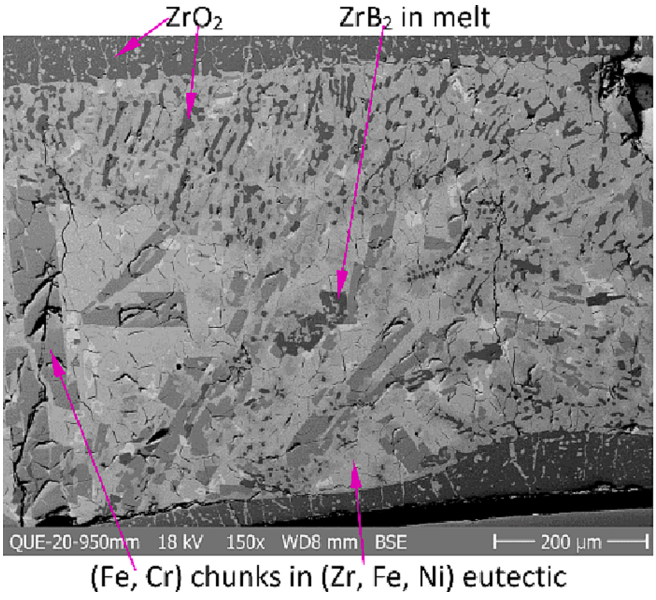


**Fig. 16.** Cladding microstructure of rod #13 (outer cladding surface at the top).

claddings of rods 13, 14 and 15 failed at the contact with the water channel and the absorber blade. The corresponding Zr/(stainless steel) eutectic melt, containing $ZrB_2$ and (Fe, Cr) chunks, penetrated underneath the cladding and distributed along the entire perimeter of the cladding under the outer oxide layer. Part of the oxide layer was dissolved and formed oxidic precipitates in the melt partially at temperature (Hofmann, 1999) and partially during melt solidification (Fig. 16).

### 4.3. *Elevation 850 mm*

Because of the failure of the cladding surface thermocouples on the inner rods at the end of transient stage, the highest cladding temperature of about 2230 K was measured during the quench stage on the surface of peripheral rod #20. Very strong degradation of the absorber blade due to melting was observed at 270°. The degree of oxidation of claddings (measured averaged ECR = 33%±7%) is higher in comparison to the elevation 950 mm, whereas the bundle oxidation gradient is similar to the 950 mm elevation (Fig. 17). The region along the absorber blades was hotter than along the two bundle sides without absorber blades. The oxide layer thickness of the central rod is relatively low due to dissolution of this layer in the melting pools formed in the bundle center.

The surrounding of the inner rods #1…#4 contains relatively low amount of metal melt because it was relocated downwards. The claddings of the other five inner rods #5…#9 consists of $ZrO_2$ and α-Zr(O) layers as well as segments of solidified metal melt (Fig. 18).

The hot peripheral rods #10…#17 along the absorber blades lost a significant part of the cladding metal melt, which relocated downward. The claddings of the relatively cold peripheral rods #18…#22 were not melted. The prior β-Zr layers of rods #23 and #24 were partially melted and include oxidic precipitates formed due to dissolution of the oxide layers by molten Zr (Fig. 19). The phenomenology of this process was investigated and described in (Hofmann, 1999). Additionally, metal precipitates are formed in the oxide due to oxygen transport to the metal (Stuckert, 2008).

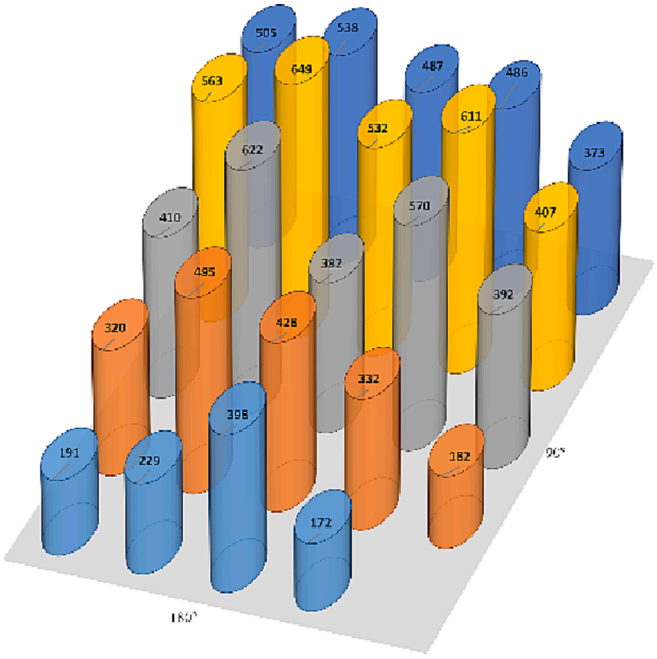


**Fig. 17.** Average thicknesses of outer $ZrO_2$ (in µm) for claddings at bundle elevation of 850 mm (top view).

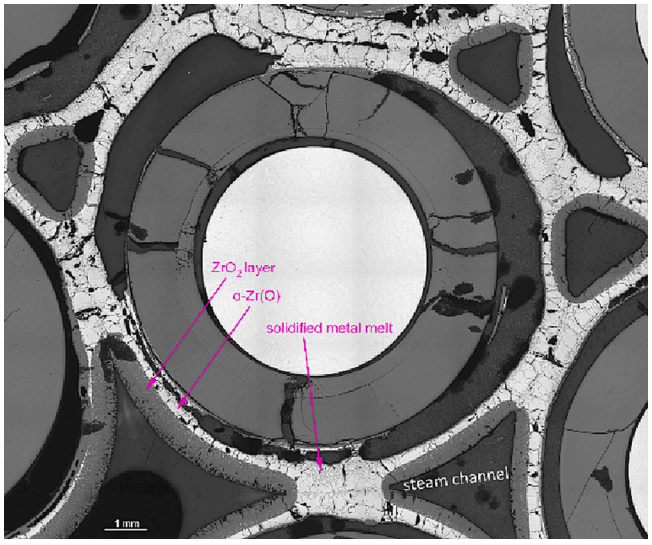


**Fig. 18.** Rod #8 at 850 mm.

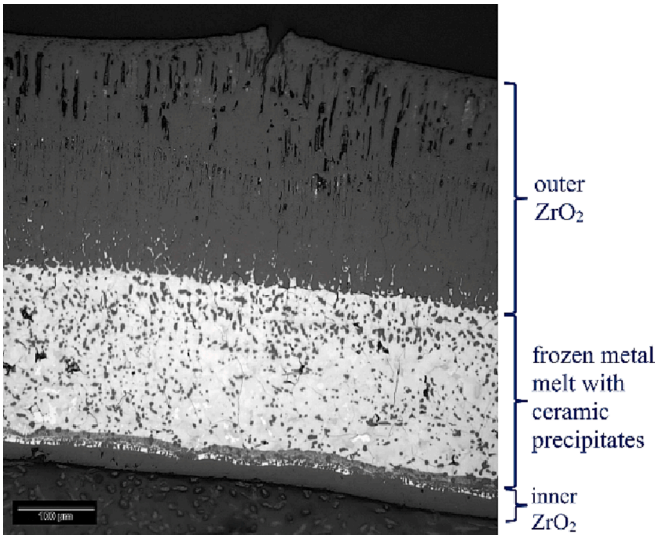


**Fig. 19.** Interaction of molten metal layer of cladding #23 with its oxide layers.

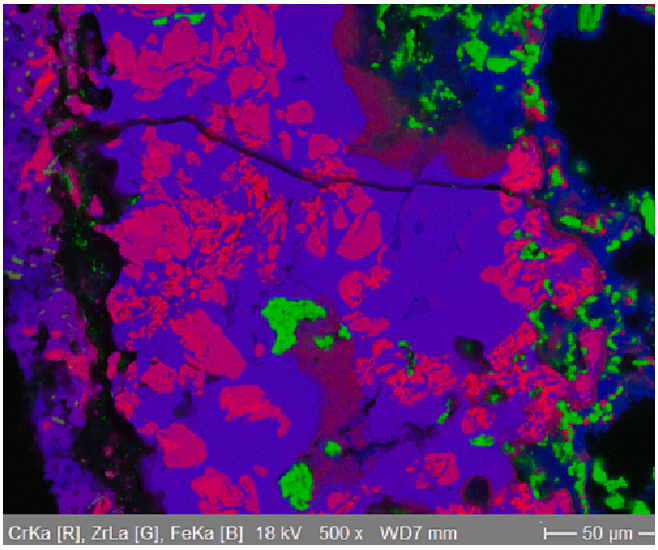


**Fig. 20.** (Fe,Cr) borides in melt near the $B_4C$ pin.

### 4.4. *Elevation 750 mm*

Due to disturbances of the cladding thermocouples, the highest temperature of 2400 K was measured by thermocouples installed at the outer surface of the shroud behind the absorber blades. Similar to 850 mm, the part of the absorber blade at the angle position 0° was spalled during the bundle dismounting, whereas the $B_4C$ pin inside the absorber blade at 270° reacted with the stainless steel of the absorber blade and was partially dissolved. The detailed SEM/EDX analysis of the eutectic melt around the $B_4C$ pin revealed the formation of equiaxed (Fe, Cr) borides near to the pins and the needle-shape $ZrB_2$ near to the Zr-based channel box (Fig. 20, Fig. 21), in full accordance with the structures observed in (Steinbrück, 2010).

The averaged equivalent cladding reacted parameter determined at this elevation is ECR = 33%±9%. The distribution of cladding oxide

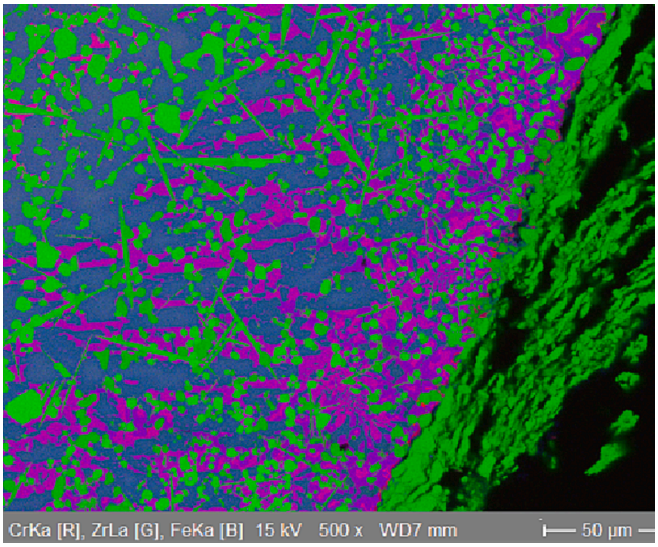


**Fig. 21.** $ZrB_2$ needles near the ZIRLO channel box.

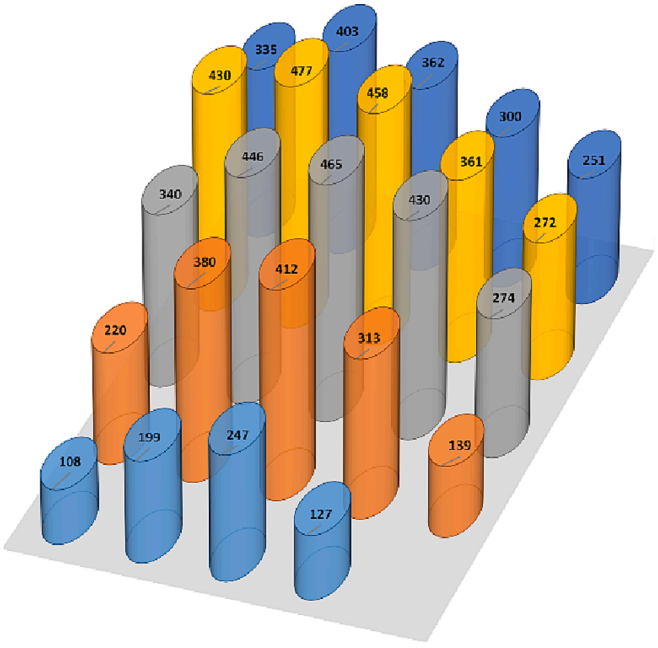


**Fig. 22.** Average thicknesses of outer $ZrO_2$ (in µm) for claddings at bundle elevation of 750 mm (top view).

layer thicknesses across the bundle has the similar gradient as for the elevations 950 and 850 mm: the degree of oxidation at the bundle sides along the absorber blades is higher in comparison to the bundle sides without blades (Fig. 22). The oxide layer thickness of the water wings was 130 μm and that of the shroud 85 μm.

The cladding melt released inside the group of the inner rods #1…#9 formed several molten pools with steam channels with oxidized edges. The pellet-cladding gaps of the inner rods #1…#4 were filled with molten metal or voids were formed here due to downwards relocation of the melt (Fig. 23). For the colder inner rods #5…#9, the gaps were mostly free of melt. For the hot peripheral rods #10…#17, the metal melt filled the entire gap and contacted the pellet (Fig. 24). The gap (formed during the lift-off of the cladding due to Kr overpressure) was free from melt for the relatively cold peripheral rods #18…#22. The claddings of the last two peripheral rods #23 and #24, which are in turn in the hot bundle area, were partially melted (especially for rod #24), and the melt contacted the pellets and the outer oxide layer.

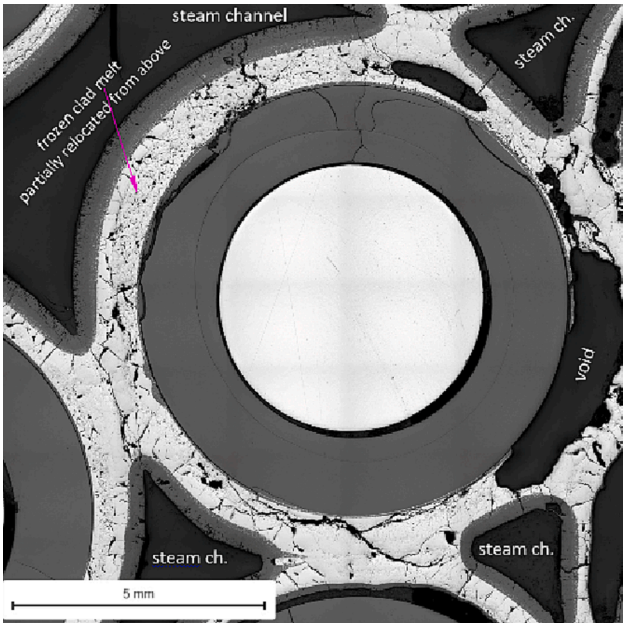


**Fig. 23.** Rod #2 at 750 mm.

### 4.5. *Elevation 650 mm*

A peak cladding temperature of about 1800 K was measured at the claddings of intermediate rods on the beginning of the quench stage. The absorber blades were significantly melted. Part of the melt was relocated also from upper elevations and attacked the $B_4C$ pins, which were partially dissolved (Fig. 25). Intense interaction of the stainless steel blade with the elements of the ZIRLO channel box and the Zr shroud was also observed.

The degree of cladding oxidation at this bundle elevation was noticeably lower than at the three elevations above: ECR = 24%±9%. While the claddings of the peripheral rods show moderate oxidation, the claddings of the central and intermediate rods were oxidized significantly (Fig. 26). Due to rather high temperatures, the oxide layer was partially dissolved by the molten β-Zr formed here and partially displaced from above.

For rods 1, 4, 7, and 8, the molten β-Zr partially moved along the pellets to lower elevations, leaving voids in their place (Fig. 27). The molten cladding β-Zr of other intermediate rods 2, 3, 5, 6, and 9 filled the gap between the outer layers and either the pellet or inner oxide layer without forming voids. In some cases, due to the lift-off of the cladding under the action of internal pressure, an increased cladding-pellet gap was formed even before the formation of the melt.

The temperatures of the claddings of the peripheral rods 10–27, located on the azimuth sides 270° and 0° of the bundle, reached the melting points of the β-Zr phase in many places due to the limited heat loss through the absorber blades. The melt formed here, together with the melt relocated from above, filled the space between the outer α-Zr (O) layer and the pellet (or inner α-Zr(O) or oxide layer). Part of the oxygen from the pellet material diffused into the melt at the points of

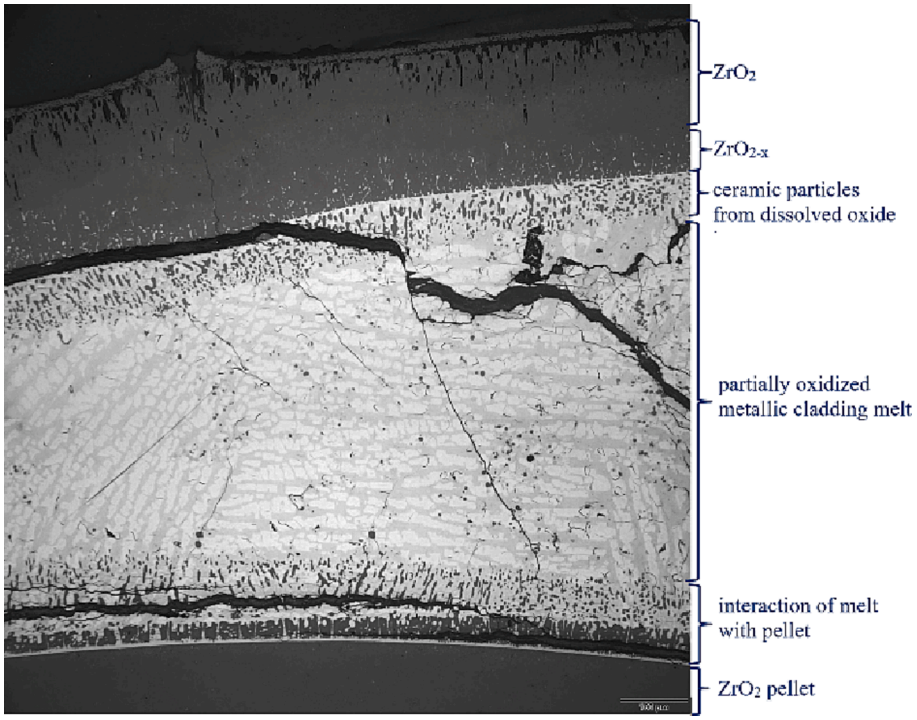


**Fig. 24.** Rod #17 at 750 mm.

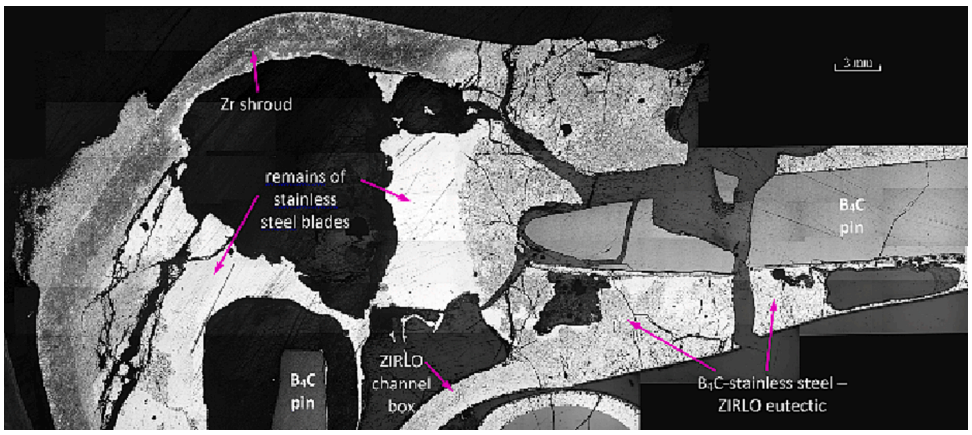


**Fig. 25.** Interaction of absorber blade with channel box and shroud.

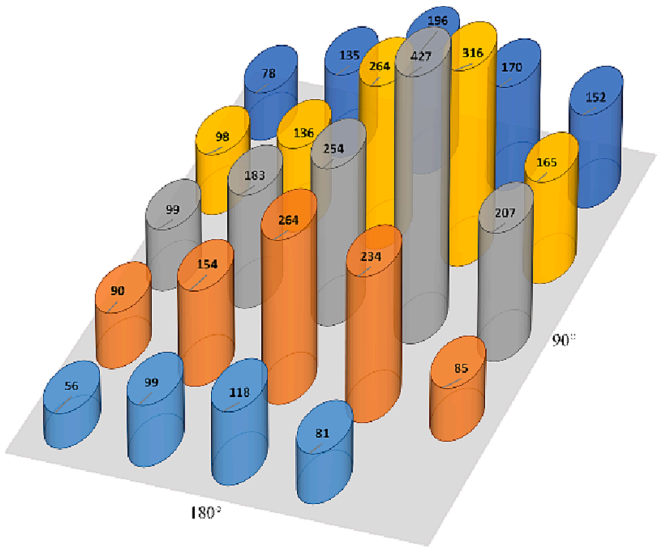


**Fig. 26.** Average thicknesses of outer $ZrO_2$ (in μm) for claddings at bundle elevation of 650 mm (top view).

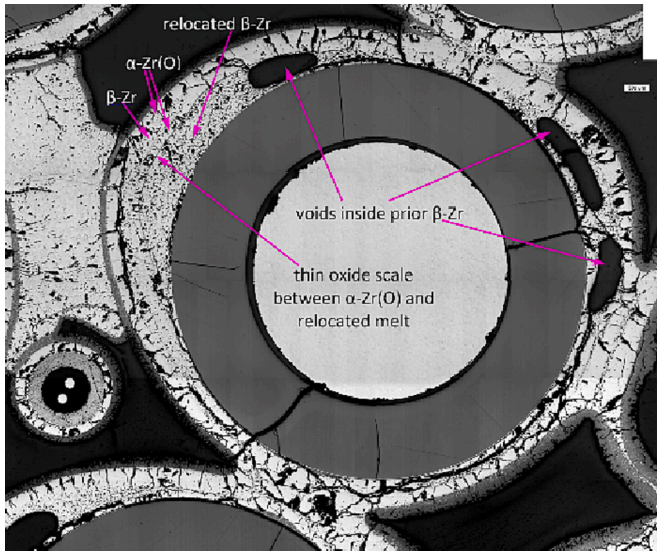


**Fig. 27.** Rod #4 at 650 mm.

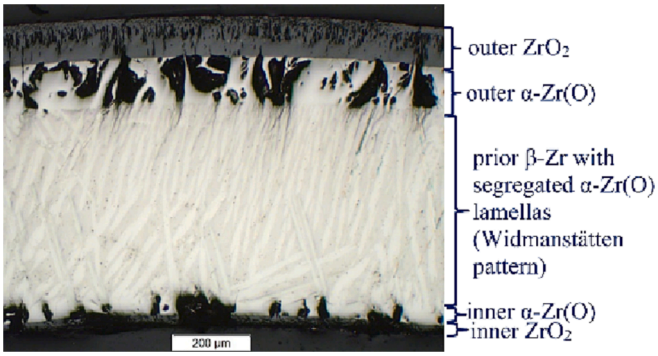


**Fig. 28.** Microstructure of cladding 23 at 650 mm.

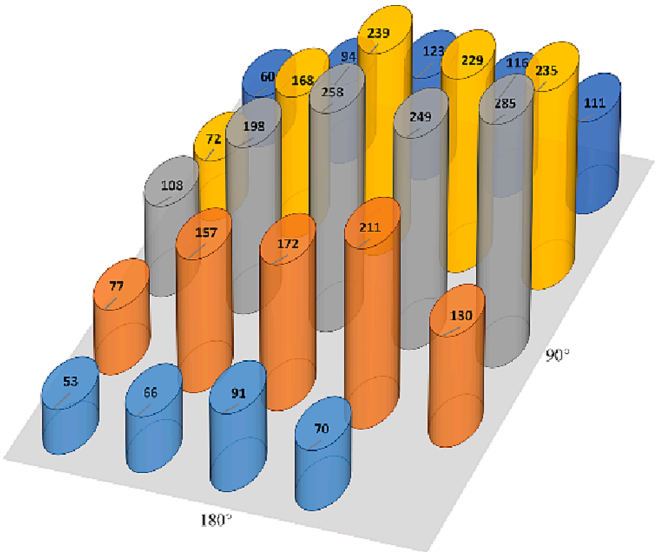


**Fig. 29.** Average thicknesses of outer $ZrO_2$ (in μm) for claddings at bundle elevation of 555 mm (top view).

contact between the melt and the pellet. As a result, the corresponding parts of the pellet acquired a characteristic dark shade, which indicates the sub-stoichiometry of the pellet material - the corresponding effect was revealed in single effect tests (Hofmann, 1999). The dark and light parts of the pellets are clearly visible in the overview image Fig. 12.

The claddings of the peripheral rods 18–24, located along the azimuth sides of the bundle 90° and 180°, did not melt and have a standard

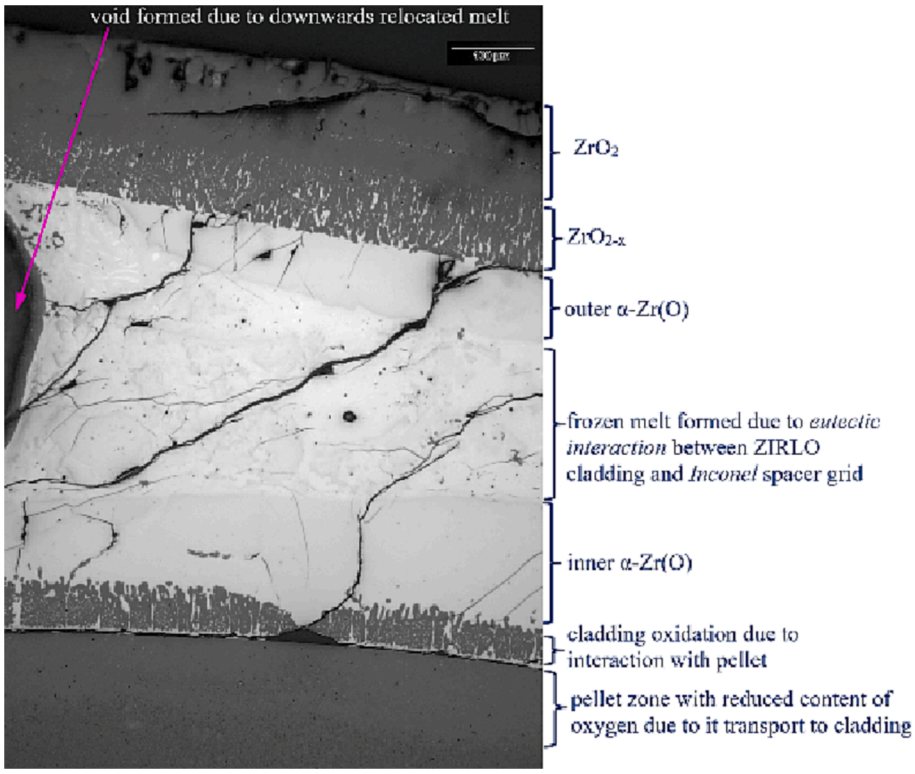


**Fig. 30.** Microstructure of rod 5 at 555 mm.

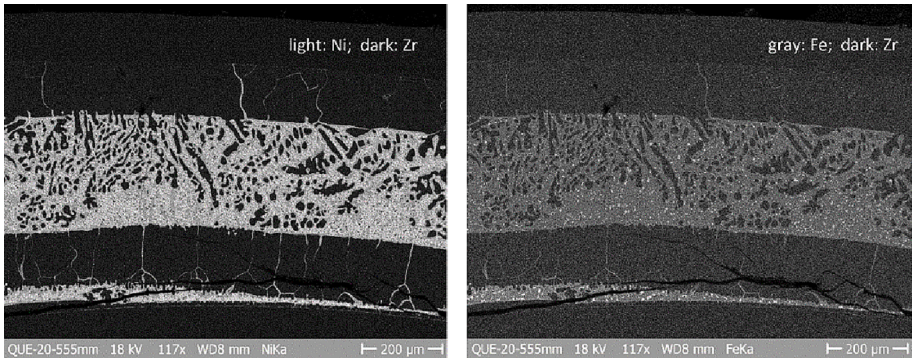


**Fig. 31.** EDX mapping of cladding 9 at 555 mm.

solid-state layer structure $ZrO_2$ - α-Zr(O) - β-Zr (with α lamellas) - α-Zr (O) - $ZrO_2$ (Fig. 28). These rods are located on two sides of the assembly, where there are no absorber blades - here the heat losses towards the shroud were higher than at the sides of the assembly with absorbers, and, respectively, the temperatures inside the rods did not reach the melting point of the cladding metal.

### *4.6. Elevation 555 mm*

Temperature peaks on the shroud (azimuthal side 0°) during the transient stage indicate the relocation of the Zr-SS eutectic melt here from the upper bundle elevations. The interaction of the melt with the $B_4C$ pins was minimal. Cladding oxidation was moderate (ECR = 15% ±4%) and more pronounced in the center of the bundle (Fig. 29).

Only small fragments of Inconel spacer grids (about 70% Ni) remained on the periphery of the bundle. In the center of the bundle, the spacer grids at these elevations were melted firstly due to the eutectic interaction of the nickel of the grids with the zirconium of the claddings: the lowest eutectic temperature in the Zr-Ni system is 1233 K. At a later stage of the transient, the melting point of the Inconel spacer (1610 K) was exceeded. The melt was partially relocated downwards, and partially penetrated under the damaged claddings.

For the central rod, even the melting point of the beta-phase layer of cladding was exceeded. The corresponding melt partially dissolved the outer oxide layer, resulting in the formation of oxidic precipitates in the melt. Similar processes were observed for the cladding of rod #4. The melt also went beyond the oxide layer and formed molten pools in the inter-rod space. For other internal rods with strong damaged claddings, the formation of an eutectic melt occurred as a result of the interaction of the Inconel spacer melt with the residual β-Zr layer of the cladding (Fig. 30). This melt is characterized by the formation of Zr precipitates distributed over the eutectic melt.

The claddings of the outer rods were less damaged than those of the inner ones, but the eutectic melt formed not only in the in the gap between the cladding and the pellet, but also between inner and outer α-Zr (O) layers. It is interesting to note that if the zirconium-nickel eutectic prevails in the melt for the more damaged inner rods, then the zirconium-iron eutectic dominates in the less damaged outer rods. This

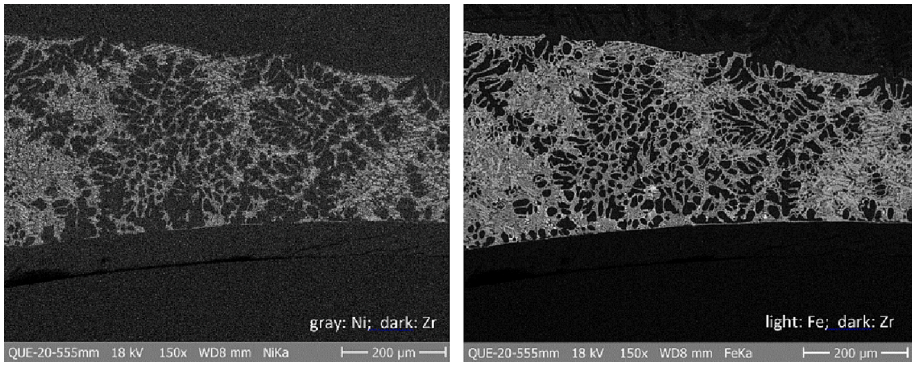


**Fig. 32.** EDX mapping of cladding 10 at 555 mm.

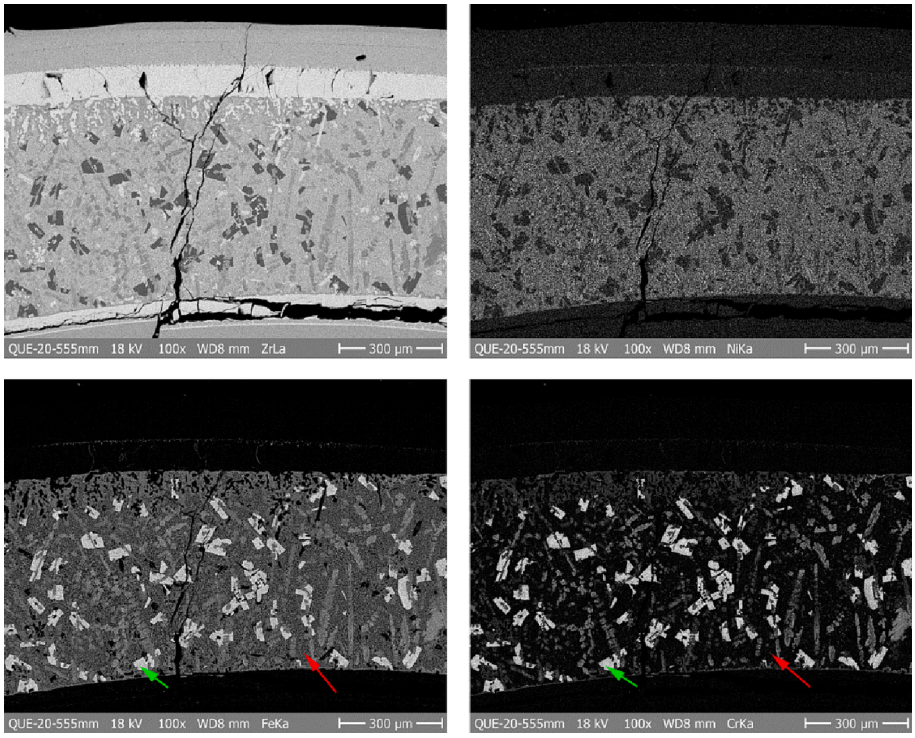


**Fig. 33.** EDX mapping of cladding 15 at 555 mm: (Fe, Cr) chunks (green arrows) in (Zr, Ni) melt (red arrows).

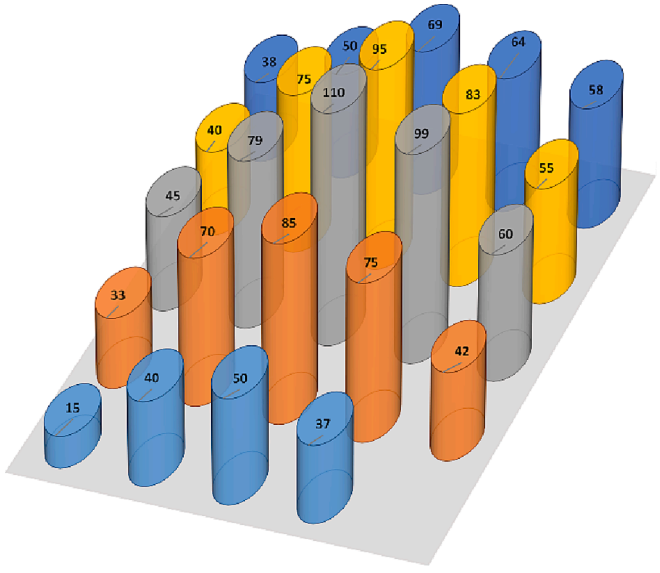


**Fig. 34.** Average thicknesses of outer $ZrO_2$ (in µm) for claddings at bundle elevation of 450 mm (top view).

is clearly seen from the comparison of the SEM/EDX analysis of rods 9 (Fig. 31) and 10 (Fig. 32). Sometimes for the outer rods, the formation of (Fe, Cr) chunks in the (Zr, Ni) eutectic melt is observed (Fig. 33).

### *4.7. Elevation 450 mm*

At this elevation, the outer layers of all claddings were not damaged. Similar to the elevation 555 mm, the degree of oxidation of the claddings (ECR = 14%±3%) can be characterized as medium (Fig. 34). Despite this, on the inner surface of almost all claddings, a eutectic nickel-containing melt is observed, which has relocated from the elevation of 550 mm along the gap between the pellets and the outer layers of the claddings (Fig. 35).

## 5. Simulation of the QUENCH-20 test with AC$^2$/ATHLET-CD

The AC$^2$/ATHLET-CD code (GRS/Germany) was used for pre- and post-test calculations (Hollands et al., 2022). The nodalization of QUENCH-20 for the simulation with ATHLET-CD is shown in Fig. 36. The main flow path is formed by an inlet, the flow channel with the bundle and the outlet.

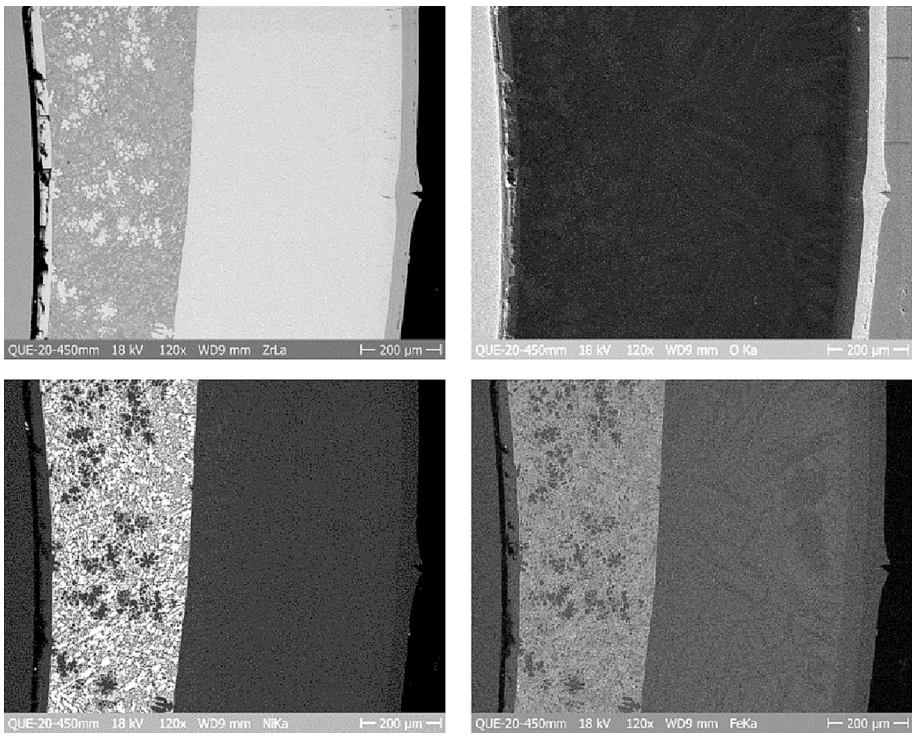


**Fig. 35.** EDX mapping of cladding 23 at 450 mm.

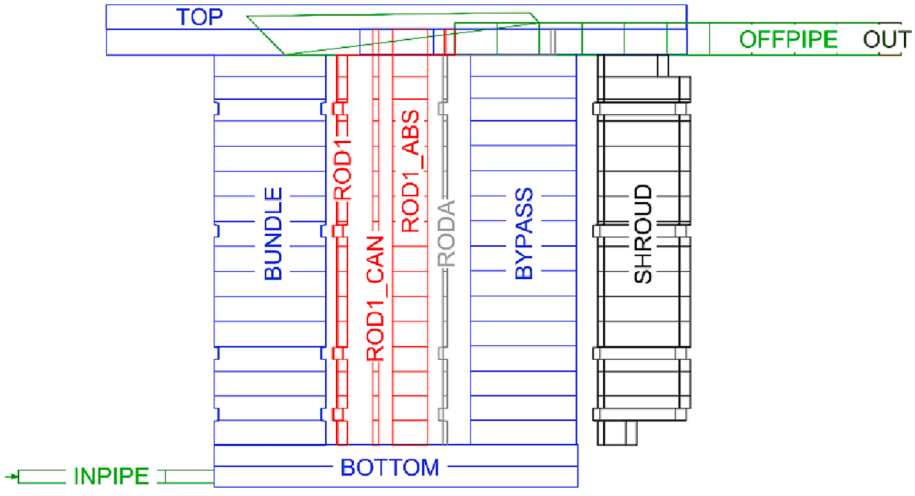


**Fig. 36.** Nodalization scheme.

The bundle is connected via cross-connections to the outer area of the heated rod bundle, whereby the surface of the bypass covers the free area lying in the area between the channel box and the shroud. The length of the test bundle represented by the structure ROD1 and its channel box (ROD1_CAN) and absorber blade (ROD1_ABS) is divided into 17 axial zones, 10 of which are in the area heated with tungsten. The cross connection between bundle and bypass opens after the channel box fails. The superheated steam, argon as carrier gas and, in the last period of the test, also the quench water flow at the lower end of the test section are supplied via the injection pipe. The steam not consumed during oxidation, argon and the released hydrogen and other gases are discharged to the outside at the upper end of the test bundle through the off-gas-pipe. The five grid spacers have been considered as thermal structures without oxidation. The pulling of the corner rod is not considered, so it contributes to the oxidation until the end of the simulation.

In general, the predicted cladding temperatures show a qualitatively and quantitatively good agreement to the measured ones. The calculated cladding temperatures at the higher elevations are in good agreement to the measured values and show only a slight overestimation at 950 mm during quenching (Fig. 37). The higher cladding temperatures at these elevations are the main driver for the temperature evolution also for the absorber blade and the channel box, while the $B_4C$ oxidation has only a minor contribution also compared to Zr oxidation of the cladding and the channel box.

In the lower and middle elevations up to 550 mm, the calculated temperatures are within the band of experimental values (Fig. 38), which is a good result due to the assumption that each single rod in ATHLET-CD has in contrast to the test the same thermal behavior. The measured peak at 550 mm is not captured by the code because the

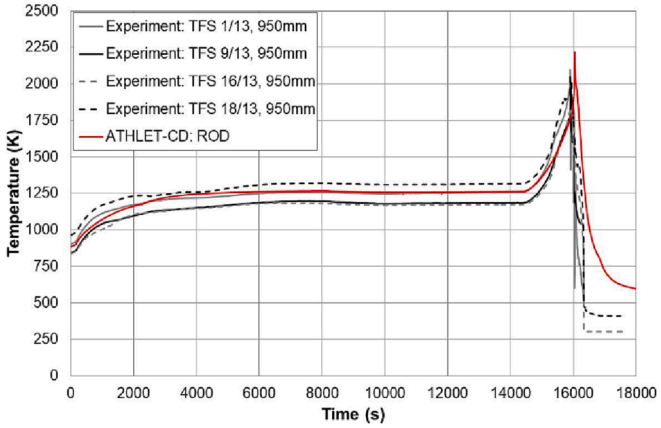


**Fig. 37.** Measured and calculated cladding temperatures at 950 mm.

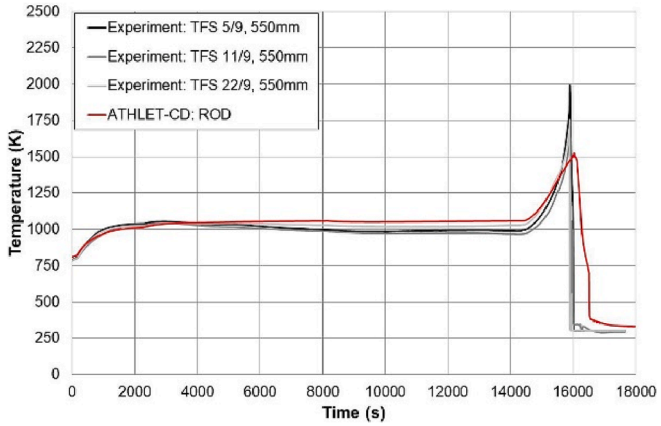


**Fig. 38.** Measured and calculated cladding temperatures at 550 mm.

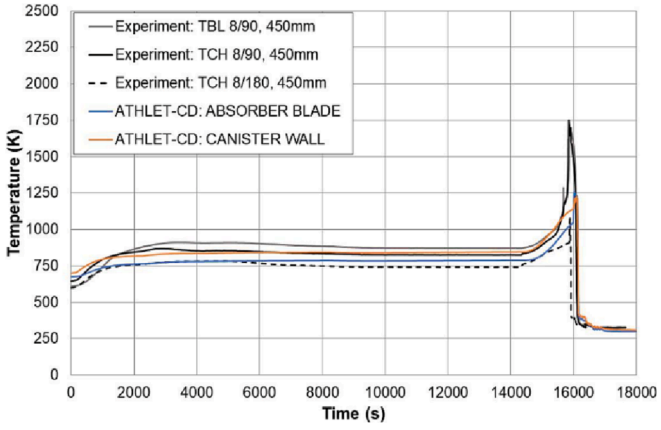


**Fig. 39.** Measured and calculated temperatures of absorber blade and channel box at 550 mm.

oxidation of BWR parts – channel box, absorber blade and $B_4C$ – is underestimated by the code and leads to a lower heat impact. Due to that, beside the rod cladding temperature also the absorber and channel box temperatures in the middle and lower elevations are underestimated (Fig. 39), because relocation of BWR structures is not calculated by the code and leads to less material for oxidation in the lower and middle bundle elevations and its heat impact. At these elevations, the measured absorber blade temperature is higher than the melting temperature of the eutectic mixture of stainless steel and boron carbide, which is not predicted by ATHLET-CD and thus leads to the underestimation of corresponding temperatures. In contrast to the experiment, the highest absorber temperatures in ATHLET-CD are calculated at higher elevations due to the missing relocation of BWR structures, but even there the melting temperature is not reached.

The total calculated hydrogen release from all components is close to the experimental value but show an overestimation during the pre-oxidation phase (Fig. 40). The probable reason of that could be overestimation of cladding temperatures at the positions of the molybdenum heaters in the head and the bottom of the bundle; similar problem took place also for the modelling with the ASTEC code (Murat et al., 2020). Totally, 44 g $H_2$ are generated, which underestimates the experimental mass (57 g) by 13 g. In the simulation, 34 g are caused by heated rods and BWR structures (11 g), while the shroud and the grids contribute 10 g. By the $B_4C$ oxidation, about 4.2 g $H_2$ are generated which underestimates the experimental value of 10 g by 58%. It could be caused by the modeling approach that the BWR oxidation is based on the modelling of PWR $B_4C$ oxidation and the considered surfaces and availability of steam needs to be further investigated. On the other hand, this underestimation of the degree of oxidation of boron carbide is associated with an underestimation of the temperatures of the control rod. Another 7.2 g of hydrogen, missing in the model compared to the experiment, indicates an underestimation of the oxidation of claddings and structural materials. This in turn due to the underestimation of the temperatures of these elements of the bundle.

Corresponding to the $B_4C$ oxidation, CO, $CO_2$ and $CH_4$ are generated and underestimated by the code in the same way as the hydrogen generation (Fig. 41).

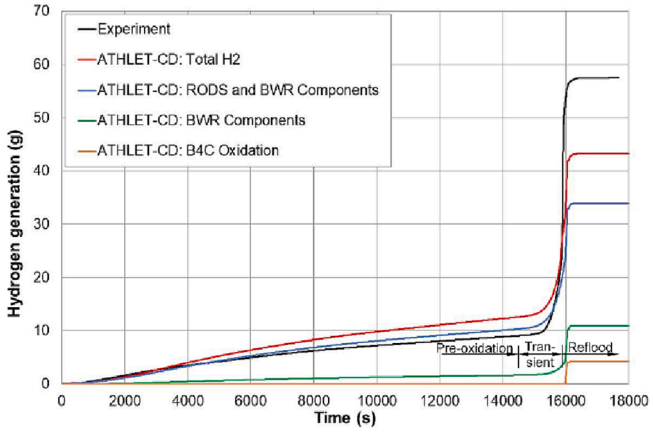


**Fig. 40.** Measured and calculated hydrogen release.

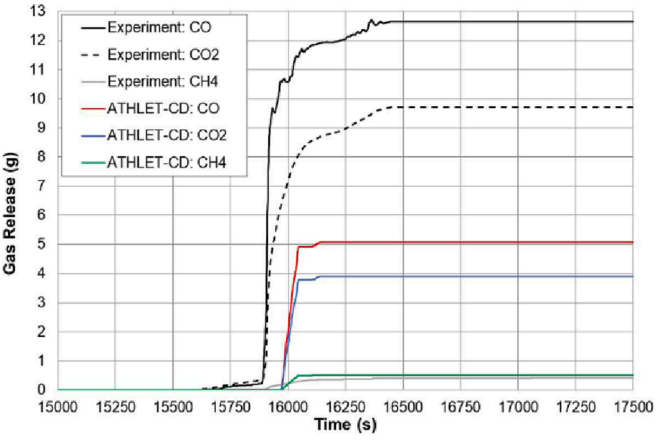


**Fig. 41.** Measured and calculated release of CO, $CO_2$ and $CH_4$.

## 6. Conclusions

The experiment QUENCH-20 with BWR geometry simulation bundle was conducted at KIT in October 2019. The test bundle mock-up represented one quarter of a BWR fuel assembly with 24 electrically heated fuel rod simulators and two stainless steel control blades filled with horizontal $B_4C$ pins. The rod simulators were filled with Kr to an inner pressure of 0.55 MPa. The pre-oxidation stage in a flowing gas mixture of steam and argon (each 3 g/s) and system pressure of 0.2 MPa lasted 4 h at the peak cladding temperature of 1250 K. The Zry-4 corner rod, withdrawn at the end of this stage, showed the maximal oxidation up to 60 μm $ZrO_2$ at elevations between 930 and 1020 mm and only 10 μm at 750 mm.

During the transient stage, the bundle was heated to a maximum temperature of 2000 K. The coolability of the bundle was decreased by its squeezing due to the shroud ductile deformation caused by an test-related overpressure outside the shroud. The cladding radial strain and failures due to inner overpressure (about 0.4 MPa) were observed at temperature about 1700 K and lasted about 200 s. During the period of rod failures, also the first absorber melt relocation accompanied by shroud failure were registered. The interaction of $B_4C$ with the steel blade and the ZIRLO channel box were observed at bundle elevations 650…950 mm with the formation of eutectic melt. The typical components of solidified melt are (Fe, Cr) borides and $ZrB_2$ precipitated in steel or in Zr-steel eutectic melt. Massive absorber melt relocation was observed 50 s before the end of transition stage. Small spillages of the absorber melt moved down to the bundle elevation of 50 mm.

Melting of Inconel spacer grids at 500 and 1050 mm was also started at the end of the transition stage. The Inconel melt from the bundle elevation 1050 mm relocated downwards through hot bundle regions to the Inconel grid spacer at 550 mm and later (during the escalation caused by quenching) to 450 mm. This melt penetrated also under the damaged cladding oxide layer and formed molten eutectic mixtures between elevations 450 and 550 mm.

The test was terminated by quench water injection with a flow rate of 50 g/s from the bundle bottom. Fast temperature escalation from 2000 to 2300 K during 20 s was observed due to the strongly exothermic oxidation reactions. As result, the metal part (prior β-Zr) of the claddings between 550 and 950 mm was melted, partially released into the space between rods and partially relocated in the gap between pellet and outer oxide layer to 450 mm. In this case, the positive role of the oxide layer should be noted, which does not allow the melt to completely escape into the inter-rod space (crucible effect). It is thereby limiting the possibility of interactions of a large amount of melt with steam, which could significantly increase the exothermic oxidation processes and the escalation of temperatures.

The oxidation degree within each bundle cross section is very inhomogeneous: whereas the average outer $ZrO_2$ layer thickness for the central rod (#1) at the elevation of 750 mm is 465 μm, the same parameter for the peripheral rod #24 is only 108 μm. The average oxidation degree of the inner cladding surface (due to interaction with steam and with $ZrO_2$ pellets) is about 20% of outer cladding oxidation. The bundle elevations 850 and 750 mm are mostly oxidized with average cladding ECR 33% due to: 1) downwards shift of the temperature maximum from 950 mm (ECR 31%) during the transient and the quench stages, and 2) due to cladding melt relocation inside and outside the rods from 800…1000 mm to lower bundle elevations. The oxidation of the melt relocated inside the rods was observed at elevations 550…950 mm.

The mass spectrometer measured the release of CO (12.60 ± 0.04 g), $CO_2$ (9.70 ± 0.03 g) and $CH_4$ (0.40 ± 0.001 g) during the reflood as products of absorber oxidation; the corresponding $B_4C$ reacted mass was 41 g or 4.6% of the total $B_4C$ inventory. It is significantly lower than in the PWR bundle tests QUENCH-07 and QUENCH-09 containing central absorber rod with $B_4C$ pellets inserted into a *thin* stainless steel cladding and Zry-4 guide tubes (20% and 50% reacted $B_4C$ correspondingly).

Hydrogen production during the reflood amounted to 32.0 ± 0.1 g during the reflood (57.40 ± 0.17 g during the whole test) including 10 g from $B_4C$ oxidation.

Pre- and post-test analyses were performed with $AC^2$/ATHLET-CD. The results of the post-test simulations show a good agreement with the experimental observations. The thermal behavior is generally well captured for the cladding, while the BWR components are underestimated especially in the middle and lower bundle heights. This could be caused by the underestimation of the $B_4C$ oxidation, which has also an exothermal character with an additional heat impact. Furthermore, melting and relocation of BWR components is not calculated, which could also have an impact on the temperatures in the lower bundle region. In this and some other tests representing BWR core, early liquefaction and relocation of control blade, and melt interaction with the channel box (even with the shroud in QUENCH-20) highlighted importance of these phenomena to be simulated in severe accident codes. More detailed experiments are needed for model development and code validation in respect to these phenomena.

## CRediT authorship contribution statement

**Juri Stuckert:** Conceptualization, Methodology, Formal analysis, Investigation, Data curation, Writing – original draft, Writing – review & editing, Visualization, Supervision. **Sevostian Bechta:** Conceptualization, Supervision, Writing – original draft, Writing – review & editing. **Thorsten Hollands:** Methodology, Software, Formal analysis, Writing – original draft. **Patrick Isaksson:** Conceptualization, Supervision, Writing – original draft. **Martin Steinbrueck:** Methodology, Formal analysis, Investigation, Writing – original draft, Writing – review & editing.

## Declaration of Competing Interest

The authors declare that they have no known competing financial interests or personal relationships that could have appeared to influence the work reported in this paper.

## Data availability

Data will be made available on request.

## Acknowledgements

The QUENCH-20 experiment was performed in the framework of the SAFEST project in cooperation with Swedish Radiation Safety Authority (SSM), Westinghouse Sweden, GRS/Germany and KTH/Sweden and supported by the KIT program NUSAFE. Special thanks goes to Ms. Korske (Westinghouse) for her help and fruitful cooperation. The bundle materials and absorbers were provided by Westinghouse Sweden.

## References

Ihsan Barin. Thermochemical Data of Pure Substances, Third Edition. VCH Verlagsgesellschaft mbH, 1995, online ISBN: 9783527619825, https://www.doi.org/10.1002/9783527619825.

S. Hagen, P. Hofmann, V. Noack, G. Schanz, G. Schumacher, L. Sepold. **Lessons learned from CORA PROGRAM**. *International Topical Meeting on Probabilistic Safety Assessment; Moving Toward Risk-Based Regulation*, Park City, Utah, September 29 - October 3, 1996.

Haste, T., Steinbrück, M., Barrachin, M., de Luze, O., Grosse, M., Stuckert, J., 2015. A comparison of core degradation phenomena in the CORA, QUENCH, Phébus SFD and Phébus FP experiments. Nucl. Eng. Des. 283, 8–20. https://doi.org/10.1016/j.nucengdes.2014.06.035.

Hering, W., Homann, C., 2007. Degraded core reflood: present understanding and impact on LWRs. Nucl. Eng. Des. 237 (24), 2315–2321. https://doi.org/10.1016/j.nucengdes.2007.04.017.

P. Hofmann, J. Stuckert, A. Miassoedov, M.S. Veshchunov, A.V. Berdyshev, A.V. Boldyrev. **$ZrO_2$ dissolution by molten Zircaloy and cladding oxide shell failure. New experimental results and modelling**. *Scientific report FZKA-6383*, 1999. https://doi.org/10.5445/IR/270046616.

Hollands, J. Stuckert, P. Isaksson, S. Bechta. **Experiment Investigation of QUENCH-T. 20 and Simulation with AC$^2$/ATHLET-CD**. 10$^{th}$ European Review Meeting on Severe Accident Research (*ERMSAR2022*). Karlsruhe, Germany, May 16-19, 2022. Paper 316.

C. Homann, W. Hering, G. Schanz. **Analysis and comparison of experimental data of bundle tests QUENCH-07 to QUENCH-09 about B4C control rod behavior.** *Scientific report FZKA-7101*, Karlsruhe, 2006, https://doi.org/10.5445/IR/270065294.

**Corrosion of Zirconium Alloys in Nuclear Power Plants.** *IAEA-TECDOC-684*, Vienna, 1993. https://www-pub.iaea.org/mtcd/publications/pdf/te_684_web.pdf.

A. Miassoedov, B. Fluhrer, C. Journeau, S. Bechta, Z. Hózer, D. Manara, P.D. Bottomley, M. Kiselová, T. Keim; G. Langrock, F. Belloni, M. Schyns. **The SAFEST project: towards pan-European Lab on Corium Behavior in Severe Accidents. Main Objectives and R&D priorities.** *ERMSAR-2017, European Review Meeting on Severe Accident Research*, Warsaw, Mai 2017.

Murat, O., Sanchez-Espinoza, V., Wang, S., Stuckert, J., 2020. Preliminary validation of ASTEC V2.2.b with the QUENCH-20 BWR bundle experiment. Nucl. Eng. Des. 370, 110931 https://doi.org/10.1016/j.nucengdes.2020.110931.

Ott, L.J., Hagen, S., 1997. Interpretation of the results of the CORA-33 dry core boiling water reactor test. Nucl. Eng. Des. 167, 287–306. https://doi.org/10.1016/S0029-5493(96)01305-2.

Pshenichnikov, A., Kurata, M., Nagae, Y., 2021. A BWR control blade degradation observed in situ during a CLADS-MADE-02 test under Fukushima Dai-Ichi Unit 3 postulated conditions. J. Nucl. Sci. Technol. 58 (9), 1025–1037. https://doi.org/10.1080/00223131.2021.1906777.

Schanz, G., Hagen, S., Hofmann, P., Schumacher, G., Sepold, L., 1992. Information on the evolution of severe LWR fuel element damage obtained in the CORA program. J. Nucl. Mater. 188, 131–145. https://doi.org/10.1016/B978-0-444-89571-4.50021-9.

Steinbrück, M., 2010. Degradation and oxidation of B4C control rod segments at high temperatures. J. Nucl. Mater. 400 (2), 138–150. https://doi.org/10.1016/j.jnucmat.2010.02.022.

Steinbrück, M., 2014. Influence of boron carbide on core degradation during severe accidents in LWRs. Ann. Nucl. Energy 64, 43–49. https://doi.org/10.1016/j.anucene.2013.09.027.

M. Steinbrück, C. Homann, A. Miassoedov, G. Schanz, L. Sepold, U. Stegmaier, H. Steiner, J. Stuckert. **Results of the B4C control rod test QUENCH-07**. *Scientific report FZKA-6746*, Karlsruhe, 2004, https://doi.org/10.5445/IR/270058023.

M. Steinbrück, A. Miassoedov, G. Schanz, L. Sepold, U. Stegmaier, H. Steiner, J. Stuckert. **Results of the QUENCH-09 experiment with a B4C control rod**. *Scientific report FZKA-6829*, Karlsruhe, 2004, https://doi.org/10.5445/IR/270059406.

Steinbrück, M., Große, M., Sepold, L., Stuckert, J., 2010. Synopsis and outcome of the QUENCH experimental program. Nucl. Eng. Des. 240 (7), 1714–1727. https://doi.org/10.1016/j.nucengdes.2010.03.021.

J. Stuckert, M. Steinbrueck, M. Grosse. **Experimental program QUENCH at KIT on core degradation during reflooding under LOCA conditions and in the early phase of a severe accident**. *Proceedings of Meeting on Modelling of Water Cooled Fuel Including Design Basis and Severe Accidents, Chengdu/China,* 2013, *IAEA TECDOC CD–1775*, pp. 281-297, http://www.iaea.org/inis/collection/NCLCollectionStore/_Public/47/035/47035567.pdf?r=1.

J. Stuckert, S. Bechta, M. Große, P. Isaksson, J. Laier, J. Moch, U. Peters, U. Stegmaier, M. Steinbrück. **Results of the QUENCH-20 experiment with BWR test bundle.** *Scientific report NUSAFE 3576*, Karlsruhe, 2022, https://doi.org/10.5445/IR/1000149400.

J. Stuckert, M. S. Veshchunov. **Behavior of Oxide Layer of Zirconium-Based Fuel Rod Cladding under Steam Starvation Conditions**. *Scientific report FZKA-7373*, 2008. https://doi.org/10.5445/IR/270071587.